buildings

MDPI

Article

Microstructural, Mechanical and Fresh-State Performance of BOF Steel Slag in Alkali-Activated Binders: Experimental Characterization and Parametric Mix Design Method

Lucas B. R. Araújo [1,2,*], Daniel L. L. Targino [1,3,*], Lucas F. A. L. Babadopulos [1], Heloina N. Costa [1], Antonio E. B. Cabral [1] and Juceline B. S. Bastos [4]

[1] Departamento de Engenharia Estrutural e Construção Civil, Universidade Federal do Ceará, Fortaleza 60440-900, Brazil; babadopulos@ufc.br (L.F.A.L.B.); heloina@crateus.ufc.br (H.N.C.); eduardo.cabral@ufc.br (A.E.B.C.)
[2] ENTPE, Ecole Centrale de Lyon, University of Lyon, CNRS, LTDS, UMR5513, 69518 Vaulx-en-Velin, France
[3] MAST-MIT, Campus Nantes, Université Gustave Eiffel, All. des Ponts et Chaussées, 44340 Bouguenais, France
[4] Department of Civil Engineering, Federal Institute of Science and Technology of Ceará, Fortaleza 60040-531, Brazil
* Correspondence: lucas.araujo@entpe.fr (L.B.R.A.); daniel.lira@univ-eiffel.fr (D.L.L.T.); Tel.: +33-(0)7-45-08-07-16 (L.B.R.A.); +33-(0)6-63-84-07-20 (D.L.L.T.)

Abstract: Alkali-activated binders (AAB) are a suitable and sustainable alternative to ordinary Portland cement (OPC), with reductions in natural resource usage and environmental emissions in regions where the necessary industrial residues are available. Despite its potential, the lack of mix design methods still limits its applications. This paper proposes a systematic parametric validation for AAB mix design applied to pastes and concretes, valorizing steel slag as precursors. The composed binders are based on coal fly ash (FA) and Basic Oxygen Furnace (BOF) steel slag. These precursors were activated with sodium silicate (Na_2SiO_3) and sodium hydroxide (NaOH) alkaline solutions. A parametric investigation was performed on the mix design parameters, sweeping the (i) alkali content from 6% to 10%, (ii) silica modulus (SiO_2/Na_2O) from 0.75 to 1.75, and (iii) ash-to-slag ratios in the proportions of 75:25 and 50:50, using parametric intervals retrieved from the literature. These variations were analyzed using response surface methodology (RSM) to develop a mechanical model of the compressive strength of the hardened paste. Flowability, yield stress, and setting time were evaluated. Statistical analyses, ANOVA and the Duncan test, validated the model and identified interactions between variables. The concrete formulation design was based on aggregates packing analysis with different paste contents (from 32% up to 38.4%), aiming at self-compacting concrete (SCC) with slump flow class 1 (SF1). The influence of the curing condition was evaluated, varying with ambient and thermal conditions, at 25 °C and 65 °C, respectively, for the initial 24 h. The results showed that lower silica modulus (0.75) achieved the highest compressive strength at 80.1 MPa (28 d) for pastes compressive strength, densifying the composite matrix. The concrete application of the binder achieved SF1 fluidity, with 575 mm spread, 64.1 MPa of compressive strength, and 26.2 GPa of Young's modulus in thermal cure conditions. These findings demonstrate the potential for developing sustainable high-performance materials based on parametric design of AAB formulations and mix design.

Keywords: alkali-activated binders; basic oxygen furnace; steel slag; high-performance; parametric analysis

check for updates

Academic Editor: Mauro Mitsuuchi Tashima

Received: 27 March 2025
Revised: 6 June 2025
Accepted: 10 June 2025
Published: 15 June 2025

Citation: Araújo, L.B.R.; Targino, D.L.L.; Babadopulos, L.F.A.L.; Costa, H.N.; Cabral, A.E.B.; Bastos, J.B.S. Microstructural, Mechanical and Fresh-State Performance of BOF Steel Slag in Alkali-Activated Binders: Experimental Characterization and Parametric Mix Design Method. *Buildings* **2025**, *15*, 2056. https://doi.org/10.3390/buildings15122056

Copyright: © 2025 by the authors. Licensee MDPI, Basel, Switzerland. This article is an open access article distributed under the terms and conditions of the Creative Commons Attribution (CC BY) license (https://creativecommons.org/licenses/by/4.0/).

1. Introduction

The construction industry has a large environmental impact [1] due to its high consumption of non-renewable materials [2] and greenhouse gas emissions [3], with ordinary Portland cement (OPC) production alone contributing 5–7% of global emissions [3]. Alkali-activated binders (AABs) offer a sustainable alternative, utilizing industrial wastes as precursors for binder manufacturing [3,4]. AABs are synthesized by combining alkaline activators, such as sodium or potassium hydroxides and silicates, with precursors like fly ash, blast furnace slag, and steel slag—industrial by-products rich in silicon, aluminum, and calcium [5–7]. For instance, common activators are sodium or potassium, hydroxides, and silicates solutions [5,8], and for precursors they are by-products or wastes such as fly ash, blast furnace, and steel slag [3,9].

The combination of precursors and activators react to form aluminosilicate and calcium silicate hydrates that may act as binders in construction materials. Those binders are viable for pastes, mortars, and even concrete applications [3,7,9], either as a partial or total replacement [8,10]. Their commercial application in pavements and structural designs was already demonstrated, for example, in the Netherlands, Czech Republic, and United Kingdom [6]. Figure 1 illustrates a general overview concerning alkali-activated binders and composites.

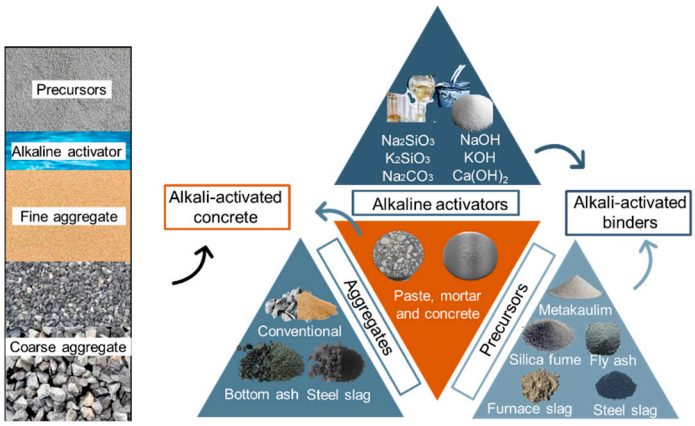

Figure 1. Schematic illustration of alkali-activated mixtures.

The type and proportion of gels formed in alkali activation, such as C-A-S-H (CaO-Al_2O_3-SiO_2-H_2O) and N-A-S-H (Na_2O-Al_2O_3-SiO_2-H_2O), depend on several factors: (i) the chemical composition of activators and precursors, (ii) activator alkalinity, (iii) curing conditions, (iv) activator-to-precursor ratios, (v) the specific surface area of precursors, and (vi) calcium and magnesium contents, among others [5,11]. Higher calcium content favors C-A-S-H formation over N-A-S-H [5,9].

The selection of precursors with varying calcium contents allows for the driven formation of N-A-S-H and C-A-S-H gels, optimizing AAB properties [5,9]. These gels significantly influence the microstructure, rheology, and strength of AABs [9]. In comparison to OPC, alkali-activated binders (AABs) may demonstrate superior chemical resistance [12,13], enhanced mechanical strength at high temperatures [14], and lower porosity [6,13]. Consequently, optimizing AABs through parametric investigation of binary precursors is a practical approach to enhance properties and mechanical performance.

The AABs design method based on chemical composition has been validated as an effective approach in the past [7,8,15,16]. This method utilizes parameters such as (i) silica modulus (S/N, which is the SiO_2/Na_2O mass ratio) and (ii) alkali content (N/B, which is the Na_2O/binder precursors mass ratio). Adjusting the ratio between sodium hydroxide and sodium silicate (which has itself a fixed silica modulus) allows for the modification

of the original SiO_2/Na_2O ratio (S/N) of the alkaline solutions [16]. Meanwhile, the N/B ratio defines the balance between activators and precursors [4,11]. The literature reports adequate compressive strength with S/N ratios between 0.5 and 2.5 [11,17,18] and N/B ranging from 4% to 15% [4,11]. For AAB concretes, mix design methods based on aggregate packing and paste content adjustment have shown good workability and strength results [8,10,19,20].

Fly ash (FA) and granulated blast furnace slag (GGBS) are widely recognized as effective precursors for AAB paste manufacturing [4,5,11]. Steel slags (SS), produced from Basic Oxygen Furnace (BOF) and Electric Arc Furnace (EAF) processes, are other potential substitutes for GGBS [21,22]. However, SS adoption is limited due to its lower amorphous silica content and high iron oxide levels, which have traditionally confined its use to soil stabilization and aggregate applications in concrete [22]. Incorporating SS in AABs presents a sustainable solution for industrial waste management, offering significant potential for large-scale implementation [22]. In 2021, global crude steel production reached 1.95 billion tons [23], generating 10–15% of by-products, much of which ends up in landfills [24]. Conversely, FA, particularly Class F with low calcium oxide content ($CaO \leq 18\%$) and high pozzolanic activity, serves as a valuable source of aluminosilicates [25]. With an annual production of 1.1 billion tons in 2016 and a utilization rate of 60% [26], combining FA with SS enables the development of AABs with enhanced rheological and mechanical performance.

Song et al. [27] investigated the use of EAF steel slag as a partial replacement for FA in mass proportions of 10%, 20%, 30%, 40%, and 50%, using sodium hydroxide and sodium silicate as activators. A 20% replacement yielded optimal results, enhancing workability, setting time, and compressive strength (25 MPa), reflecting the binders' influence on the composites. Cristelo et al. [28] examined steel slag both as precursor and aggregate in alkali-activated mortars based on FA activated with sodium hydroxide. Their findings indicated that a 50% replacement for the precursor and 100% for the aggregate led to a compressive strength of 28 MPa at 28 days. Adesanya et al. [29] evaluated the mechanical and durability properties of pastes and mortars using ladle steel slag as a precursor, activated with solid potassium hydroxide and sodium silicate. Compressive strength values reached 62 MPa for pastes and 67 MPa for mortars at 28 days.

While the referred studies provide valuable insights into the mechanical performance of alkali-activated composites, comprehensive investigations into the interaction between AAB pastes and concrete mix design remain limited. There is a gap in research addressing fresh-state consistency and strength evolution over time [30,31]. Furthermore, studies specifically focused on alkali-activated materials incorporating FA and SS are still in their early stages and often fail to integrate findings on paste and concrete applications [21,22,28].

This study conducted a systematic parametric validation to investigate and optimize AABs and demonstrated the potential application of BOF steel slag as a precursor for AABs. The intended use is for structural applications, in such a way that comparisons of AAB and OPC are given when necessary, as well as being a study on concrete, for validation. The systematic parametric study investigated the effects of silica modulus (S/N), alkali content (N/B), binary precursor proportions, and curing processes on key performance parameters. The research aimed to evaluate key parameters influencing performance on setting time, flowability, and compressive strength, as well as the influence of curing conditions on strength development. Mechanical and rheological properties were assessed through compressive strength, static Young modulus, mini-slump flow, and setting time. Microstructural features were evaluated by scanning electron microscopy coupled with energy-dispersive X-ray spectroscopy (SEM/EDS), and supported by previous findings based on X-ray diffraction (XRD) tests on similar materials. This is aligned with the literature on the subject. A parametric mix design method was proposed, leveraging

the chemical composition of precursors and activators to optimize binder formulations. For concrete applications, the packing analysis method was employed to determine the aggregate-to-paste content ratio and the aggregate proportion as well, achieving high fluidity and compressive strength. By addressing both fresh- and hardened-state properties, the study sought to validate the feasibility of using BOF steel slag in high-performance AABs and establish its potential as a scalable, sustainable alternative to OPC. The proposed design framework addresses the current gap in systematic mix design procedures for alkali-activated binders to support the development of performance-oriented binders, aiming at structural applications. Also, it enables the use of steel slag as a chemically viable precursor, demonstrating its applicability in structural-grade, low-carbon concrete systems.

2. Materials

The AAB pastes were prepared using a binary mixture of FA and BOF steel slag (SS), both sourced from a local industrial plant in Ceará, Brazil. Sodium hydroxide and sodium silicate solutions, obtained commercially, were used as alkaline activators. Paste and concrete specimens were cast to validate the proposed mix design procedure.

Both precursors were mechanically crushed and sieved to achieve a particle size below 150 μm, enhancing reaction kinetics, binder formation, and quality control [9,11]. The FA exhibited a specific gravity of 2.341 g/cm^3 and a specific surface area of 4790 cm^2/g, while the SS had corresponding values of 3.127 g/cm^3 and 3360 cm^2/g. These parameters, particularly the specific surface area, directly influence the demand for activator solutions and reaction kinetics. Compared to the literature, the FA presented a higher surface area, while the SS values were lower. Lee and Lee [15] reported 2900 cm^2/g and 4850 cm^2/g, and Li et al. [4] documented 2900 cm^2/g and 4460 cm^2/g for FA and SS, respectively. This was attributed to differences in the manufacturing used to obtain these materials. The lower BOF surface area is attributed to its angular morphology and higher crystallinity.

Laser particle size distribution (PSD), analyzed with a Shimadzu SALD-2300, revealed an average particle diameter of 5.6 μm and a maximum size of 106.9 μm for FA, whereas SS showed an average of 35.4 μm and a maximum of 141.0 μm. X-ray fluorescence (XRF) analysis using a Rigaku ZSX Mini II provided the oxide compositions listed in Table 1.

Table 1. Chemical composition of precursors by XRF.

Material	Al_2O_3	SiO_2	P_2O_5	SO_3	Cl	K_2O	CaO	TiO_2	MnO	Fe_2O_3
BOF Steel slag precursor (%m.)	1.94	5.64	0.84	0.83	0.04	0.14	53.14	-	2.97	34.40
BSSF Steel slag aggregate (%m.)	0.70	4.78	0.96	-	0.01	0.05	40.46	0.42	4.13	50.14
Fly ash (%m.)	11.14	42.17	0.53	1.08	0.06	3.97	10.25	2.74	0.27	26.98

The FA, Class F, contained 11.14% Al_2O_3, 42.17% SiO_2, and 10.25% CaO, with a sum of SiO_2, Al_2O_3, and Fe_2O_3 content exceeding 50% and CaO below 18%, indicating pozzolanic activity [32]. Fe_2O_3 content in FA is known to vary depending on the coal's origin. In the case of the material sourced in this study, the coal is derived from anthracite and bituminous reserves rich in Fe_2O_3. Consequently, both precursors exhibited elevated Fe_2O_3 levels, which may inhibit the formation of C-A-S-H gels in high-calcium AABs or substitute Al^{3+} in octahedral disposition in low-calcium systems [8]. To further investigate these effects, SEM images of the precursors are presented in Figure 2, highlighting their morphology within its possible influence on the AAB formation.

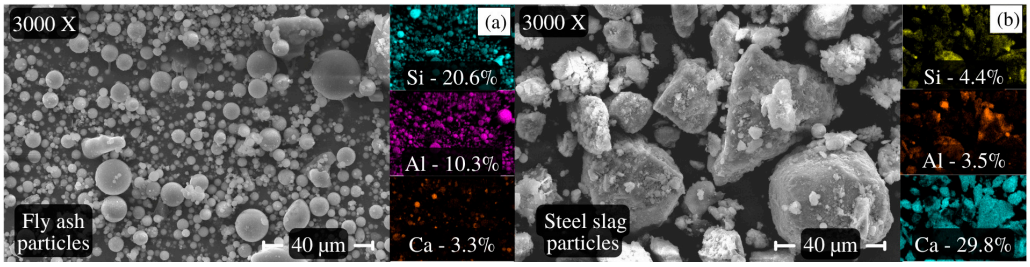

Figure 2. SEM images of precursor: (**a**) fly ash; (**b**) BOF.

FA particles present a spherical morphology finer than the angular particles of SS. Energy dispersive spectroscopy (EDS), conducted alongside SEM analysis, provided estimates of calcium, silicon, and aluminum contents. The higher calcium content in SS has an influence on the formation of C-A-S-H and N-A-S-H during alkali activation [9]. The sodium hydroxide solution was used in a 10 mol/L concentration, consisting of 31.3% hydroxide and 68.7% water by mass, aligning with the proportions reported by Rafeet et al. [16]. This concentration, selected based on the literature [33], had a specific gravity of 1.305 g/cm^3. Sodium silicate had a chemical composition of 14.98% Na_2O, 31.83% SiO_2, and 53.19% H_2O by mass, with a specific gravity of 1.575 g/cm^3.

3. Systematic Parametric Validation and Compressive Strength Response Surface Methodology (RSM)

3.1. Methodology Abstract

The schematic representation of the mix design methodology in Figure 3 encompasses two stages: the paste production and the concrete formulation. While grounded in the existing literature [4,10,11,16–18,34], it advances by introducing a parametric mix design approach to achieve the binders' strength and consistency requirements.

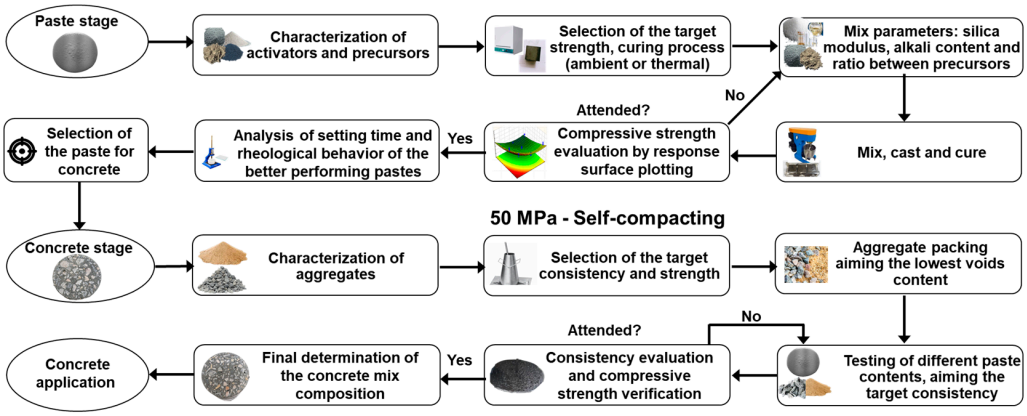

Figure 3. Mix design procedure of alkali-activated pastes and concrete.

The mix design process is organized into two sequential stages. The first stage focuses on binder formulation, which is based on the chemical and physical characteristics of the precursors and activators, the curing conditions, and the target compressive strength and workability. Once the paste composition is established, the second stage involves the development of the concrete mixture. This phase includes optimizing aggregate packing and adjusting the paste volume to ensure the desired mechanical performance and fresh-state properties are achieved.

The paste mix design procedure was based on a parametric investigation to assess the relationship between the silica modulus (S/N) and alkali dosage (N/B) with key output parameters, particularly compressive strength. The approach involved systematic variation

of S/N in the range of 0.5 to 2.5 [11,17,18] and N/B from 4% to 15% [4,11], aiming to identify optimal combinations and to enable a comprehensive understanding of their effects on the performance of the alkali-activated system.

Precursor ratios were adjusted to achieve optimal Si/Al ratios (ranging from 1 to 3) and to regulate calcium content, ensuring a balance between setting time and microstructural development [9,35]. Curing conditions included ambient curing at 25 °C (65–85% RH) and thermal curing at 65 °C for 24 h, both employed to promote early gel formation and enhance strength development [29,34,36]. The experimental boundaries, summarized in Table 2, were defined to assess the influence of these variables on compressive strength and setting time within the proposed parametric framework.

Table 2. Binder mix design experimental verification, 36 combinations.

Parameters	Min.	Max.	Var.	Total
S/N (ad)	0.75	1.75	0.5	3
N/B (%)	6.0	10.0	2.0	3
Precursors (FA-SS)	75-25	50-50	-	2
Curing Method	Ambient (25 °C)	Thermal (65 °C)	-	2

Paste formulations were cast and tested for compressive strength at 28 days. The results were analyzed using response surface methodology (RSM), which enabled the development of a response model correlating compressive strength with silica modulus (S/N) and alkali dosage (N/B). Their visual characteristics, illustrating homogeneity and consistency, are presented in Figure 4.

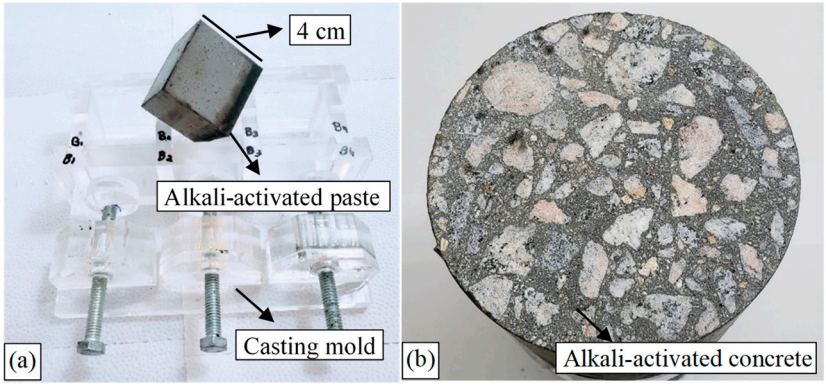

Figure 4. Alkali-activated materials aspect: (**a**) AAB pastes; (**b**) AAB concretes.

Based on the results, the paste formulations that exhibited the highest compressive strength were replicated for complementary tests, including rheological and setting time evaluations, to assess fresh-state behavior. Compressive strength was additionally monitored at 7, 14, and 28 days. The minimum recommended setting time for alkali-activated binder (AAB) pastes was 45 min, with an optimal duration exceeding 150 min to accommodate transportation, production, and molding operations [37,38].

For concrete applications, additional parameters were considered: (i) aggregate characterization—including specific and apparent specific gravity, water absorption, void content, and particle size distribution (PSD); (ii) determination of optimal fine-to-coarse aggregate ratios based on packing density and void content analyses; (iii) compressive strength and consistency requirements; and (iv) estimation of paste content in the fresh state, based on the aggregates' void content. A 10% margin was added to the calculated paste content to ensure adequate fluidity [10,16,34]. The appearance of the cast alkali-activated concretes is presented in Figure 4.

Concrete strength is influenced by the interfacial transition zone (ITZ), often resulting in lower values compared to binder-only systems [7,39]. During mix preparation, the binder content was adjusted in 5% increments to achieve the target consistency (SF1 class). Once the formulation parameters were defined, concrete specimens were cast in triplicate.

3.2. Systematic Parametric Validation for AAB Pastes

A systematic parametric validation was conducted to assess the influence of silica modulus (S/N), alkali dosage (N/B), and curing conditions on the compressive strength of AAB pastes, exploring a parameter range from the literature's recommendations [4,11,17,18,40]. A total of 18 formulations were cast into two curing conditions and evaluated for compressive strength at 28 days. The compressive strength threshold was 50 MPa for ambient curing and 60 MPa for thermal curing. S/N, N/B, and curing conditions were varied within the bounds specified in Table 2. The details of each formulation are outlined in Table 3.

Table 3. Formulations design for systematic parametric validation.

Paste ID	FA-SS	S/N [1]	N/B [2]	Sodium Hydroxide		Sodium Silicate		Fly Ash		Steel Slag		A/B [3]
				kg/m^3	% vol.	kg/m^3	% vol.	kg/m^3	% vol.	kg/m^3	% vol.	% mass
1	75-25	0.75	6.0	261.1	20.0	230.6	14.6	1223.3	52.3	407.8	13.0	30.1
2	75-25	0.75	8.0	312.0	23.9	275.6	17.4	1096.5	46.8	365.5	11.7	40.2
3	75-25	0.75	10.0	353.4	27.1	312.1	19.7	993.5	42.4	331.2	10.6	50.2
4	75-25	1.25	6.0	162.1	12.4	374.9	23.7	1193.3	51.0	397.8	12.7	33.7
5	75-25	1.25	8.0	192.8	14.8	445.9	28.2	1064.5	45.5	354.8	11.3	45.0
6	75-25	1.25	10.0	217.5	16.7	503.1	31.8	960.8	41.0	320.3	10.2	56.2
7	75-25	1.75	6.0	67.8	5.2	512.3	32.4	1164.7	49.8	388.2	12.4	37.4
8	75-25	1.75	8.0	80.2	6.1	606.6	38.3	1034.3	44.2	344.8	11.0	49.8
9	75-25	1.75	10.0	90.2	6.9	681.9	43.1	930.2	39.7	310.1	9.9	62.3
10	50-50	0.75	6.0	273.1	20.9	241.2	15.2	852.9	36.4	852.9	27.3	30.1
11	50-50	0.75	8.0	324.8	24.9	286.9	18.1	760.9	32.5	760.9	24.3	40.2
12	50-50	0.75	10.0	366.5	28.1	323.7	20.4	686.8	29.3	686.8	22.0	50.2
13	50-50	1.25	6.0	169.3	13.0	391.6	24.7	831.1	35.5	831.1	26.6	33.7
14	50-50	1.25	8.0	200.4	15.4	463.6	29.3	737.8	31.5	737.8	23.6	45.0
15	50-50	1.25	10.0	225.2	17.3	521.0	32.9	663.4	28.3	663.4	21.2	56.2
16	50-50	1.75	6.0	70.7	5.4	534.6	33.8	810.3	34.6	810.3	25.9	37.4
17	50-50	1.75	8.0	83.3	6.4	629.9	39.8	716.1	30.6	716.1	22.9	49.8
18	50-50	1.75	10.0	93.3	7.2	705.4	44.6	641.5	27.4	641.5	20.5	62.3

[1] S/N: Silica modulus (SiO_2/Na_2O, mass ratio), [2] N/B: Alkali content (Na_2O/binder precursors, mass ratio), [3] A/B: Activator solution to binder precursor ratio.

The curing process was carried out both under ambient and thermal conditions. Compressive strength results were analyzed using Statistica V10® software, with outliers identified and excluded based on standardized residuals (2 of 126 data points). Analysis of variance (ANOVA) was applied to determine the influence and significance of the design parameters. For the other tests in the fresh and hardened state, only the standard deviations of the results were assessed.

Those three formulations exhibiting the highest compressive strengths were additionally replicated to assess fresh-state with monotonic flowability and setting time tests (mini-slump) [38,40]. Fresh-state evaluations aimed to identify formulations combining strength with fluidity, which are crucial for concrete applications [8]. This approach has been extended to alkali-activated systems by Roussel and Coussot [41] and Tan, Bernal, and Provis [42], allowing yield stress estimation. The yield stress calculation is performed by Equation (1).

$$\tau_0 = \frac{225\rho g \Omega^2}{128}\pi^2 R^5 \quad (1)$$

Whereas τ_0 = yield stress [Pa]; ρ = paste density at fresh state [kg/m^3]; g = gravity acceleration (9.81) [m/s^2]; Ω = volume of the mini-slump apparatus [m^3]; R = spread radius [m].

The optimized paste formulation exhibiting high compressive strength and high fluidity properties was applied to concrete production. It was aimed at overcoming a compressive strength of 50 MPa with SSC SF1 class behavior [43]. This is a concern for AAB applications in terms of flowability and consistency in the fresh state [10,16].

3.3. Concrete Formulation and Binder Content Optimization

Aggregate packing analysis determined the optimal ratio for coarse aggregates, comprising 40% of 4.75–12.5 mm particles and 60% of 9.5–25 mm particles, achieving a void content of 41.37%, consistent with findings from Rafeet et al. [16]. This method was extended to fine aggregates, identifying a proportion of 35% to 65% fine-to-coarse aggregate, resulting in a void content of 31.95%, comparable to Bondar et al. [19]. The binder content was adjusted to 33.6% (5% above the void content), 35.2% (10%), 36.8% (15%), and 38.4% (20%), aligning with Bernal et al. [44], Rafeet et al. [16], and Bondar et al. [19], with contents between 30% and 40%.

Initial consistency verification was performed via slump tests [45], targeting a slump value higher than 270 mm. Upon achieving this level, specimens underwent slump flow and T50 testing (time required for a 50 cm spread) [46] to confirm consistency and fluidity suitable for SCC. The selected paste formulation for concrete application featured an S/N of 10%, an N/B of 0.75, and a fly ash-to-steel slag ratio of 75:25. The paste was selected based on its superior mechanical and workability properties, which are crucial for casting concrete without mechanical vibration. In addition, the paste content was set at 38.4% (20% above the void content), ensuring sufficient binder volume for optimal workability and mechanical performance. The binder-to-aggregate ratio for all concrete mixtures was 1:3, by mass. Details of the concrete formulation are provided in Table 4.

Table 4. AAB concrete formulation.

Materials	(kg/m^3)	% vol.
Fly Ash	382.1	16.3
Steel Slag prec.	127.4	4.1
NaOH (solution)—10 mol/L	135.9	10.4
Na_2SiO_3 (solution)	120.1	7.6
Fine aggr.	561.6	21.8
Coarse aggr. 4.75–12.5 mm	417.2	16.0
Coarse aggr. 9.5–25 mm	625.8	23.8

3.4. Specifics on Mixing, Specimen Manufacturing, Curring Conditions and Testing Procedure

3.4.1. AAB Paste

AAB pastes were prepared using a planetary mixer with a 1.5 L capacity, also operating at a speed of 62 ± 5 rpm. The 10 mol·L^{-1} NaOH solution was prepared 24 h in advance, while the complete activator solution—comprising NaOH and sodium silicate—was mixed 1 h prior to use. The dry precursors were manually pre-homogenized for 60 s before the activator solution was added. The mixture then underwent mechanical mixing for 90 s, followed by a 60-s resting period to verify homogenization. A final low-speed mixing stage of 90 s was performed to complete the paste preparation process.

Ambient curing was conducted at 25 ± 2 °C and 65–85% relative humidity for up to 28 days. Thermal curing specimens were placed in an oven at 65 °C for 24 h immediately after casting to accelerate early strength development. After this period, they were trans-

ferred to ambient curing conditions for the remainder of the curing time. After demolding, all specimens were stored at room temperature (25 °C) until testing.

Pastes were cast in triplicate into acrylic prismatic molds (40 × 40 × 160 mm) in two layers and compacted on a vibrating table over 30 s. Compressive strength was evaluated on these specimens using a universal testing machine (300 kN capacity) at a loading rate of 500 ± 50 N/s [47]. The three formulations yielding the highest compressive strength were selected for additional characterizations, including mini-slump flow, initial/final setting time measurements [38,40] and microstructural analyses. Microstructural features were evaluated by scanning electron microscopy coupled with energy-dispersive X-ray spectroscopy (SEM/EDS).

To minimize variability associated with raw material heterogeneity and environmental conditions, all procedures were conducted under controlled laboratory conditions, with careful documentation and triplicate testing throughout the experimental program.

3.4.2. AAB Concretes

AAB concrete batches were prepared in a free-fall mixer with a 24 L capacity, operating at a speed of 62 ± 5 rpm. Initially, the coarse aggregates were mixed with 10% of the total activator solution for 120 s. Subsequently, the precursors—manually pre-homogenized for 60 s—and 80% of the activator solution were added and mixed for 180 s. Then, the fine aggregates were incorporated and mixed for an additional 180 s. Finally, the remaining 10% of the activator solution was added, followed by a final mixing stage of 120 s. Concretes were cast in triplicate into plastic cylindrical molds (10 × 20 mm, diameter × high) in two layers molded with 12 stabs by layer, with a 16 mm diameter compacting bar. The concrete samples were subjected to both ambient and thermal curing, following the same procedure applied to the paste samples.

Fresh-state properties were assessed through slump and slump flow tests following the standards procedures [45,46]. Specimens were then cast in triplicate into cylindrical PVC molds (100 × 200 mm) for compressive strength [48] and static Young's modulus [49] testing. Compressive strength was measured using a universal testing machine (1000 kN capacity) at a loading rate of 0.45 ± 0.15 MPa/s. The modulus of elasticity was calculated from stress–strain data, based on the stress corresponding to 30% of the average compressive strength. Additional characterizations included bulk density and open porosity, SEM/EDS and, supported by previous findings in similar materials, X-ray diffraction (XRD). XRD was performed using a Quanta 450 FEG—FEI system, and analyzed with PANalytical X'Pert PRO software, with scanning performed in the range of 3° to 100° (2θ), utilizing a step size of 0.013°.

4. Results and Discussions

4.1. Systematic Parametric Validation and Paste Compressive Strength SRM

4.1.1. Pastes Compressive Strength Results

The compressive strength results of the systematic parametric validation are presented in Figure 5. Formulations with an N/B ratio of 6% (1, 4, 7, 10, 13, and 16) presented the highest strengths for thermal curing. This ratio provided an optimal balance of N/B for effective activation while maintaining a low water-to-binder ratio (68.7% of water content in NaOH and 53.2% in Na_2SiO_3), and consequently a low void content. This contributed to the improved mechanical performance above 50 MPa, in agreement with findings in the literature [10]. However, this 6% N/B ratio exhibited low fluidity not feasible for the casting process and unsuitable for concrete applications.

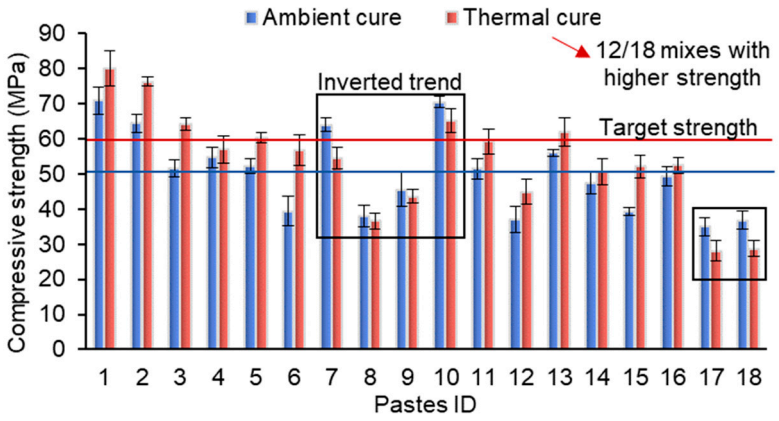

Figure 5. Compressive strength results at 28 days for AAB pastes parametric validation.

Under ambient curing, nine formulations surpassed the 50 MPa requirement, and seven exceeded 60 MPa under thermal curing. These compressive strength results were achieved even with a 50% incorporation of steel slag as a precursor, highlighting its potential for use in alkali-activated binder [50]. The highest strength was by formulation 1 (S/N of 0.75, N/B of 6%, and an ash-to-slag ratio of 75:25), with 70.9 MPa under ambient conditions and 80.1 MPa under thermal conditions. This formulation exceeded similar formulations from the literature for ambient temperature curing, which typically reached 25 MPa. For thermal curing, strength gains were moderate compared to previous studies, with 60 MPa on average [27,29,51]. This was an indication of the feasibility of the proposed approach and methodology.

Despite the general trend of increased strength with thermal curing, six outcomes exhibited an inverse relationship and formulations with a 1.75 S/N ratio. This behavior is attributed to the higher SiO_2 content, derived from the sodium silicate, which has a crucial role in the formation of a three-dimensional polymeric network. This directly influences the phase transitions during the alkali activation process by promoting rapid microstructural development at early ages [11,52]. Similar observations were reported by Soutsos et al. [11] for FA-GGBS blends at a 40:60 ratio cured at 20 °C versus 70 °C, suggesting that ambient conditions may better preserve strength in some cases.

4.1.2. Paste Compressive Strength RSM Model

Based on the results presented in Figure 5 and the specifics in Table 3, response surface models (RSM) were constructed for compressive strength, presented in Figure 6. They investigate the influence of N/B, S/N, ash-to-slag ratios, and curing conditions. These models illustrate how parameter interactions impact strength, with plots segmented by precursor ratios (FA-SS 75:25 and 50:50) and curing methods (ambient and thermal). Compressive strength outcomes are in the z-axis, plotted in color scale.

The silica modulus (S/N) demonstrated a significant impact on compressive strength, with lower S/N values (0.75) yielding the highest results. This deviates from trends observed in FA-GGBS blends, where optimal strengths occur at ratios between 1.25 and 2.5 [8,53]. This underscores the distinct behavior of BOF slag, which cannot be directly equated to GGBS due to differences in its chemical composition, particularly its high Fe_2O_3 content [4,5,11]. The role of Fe_2O_3 content in AABs remains insufficiently studied, with the need for further investigation to clarify its influence on gel formation [8,54].

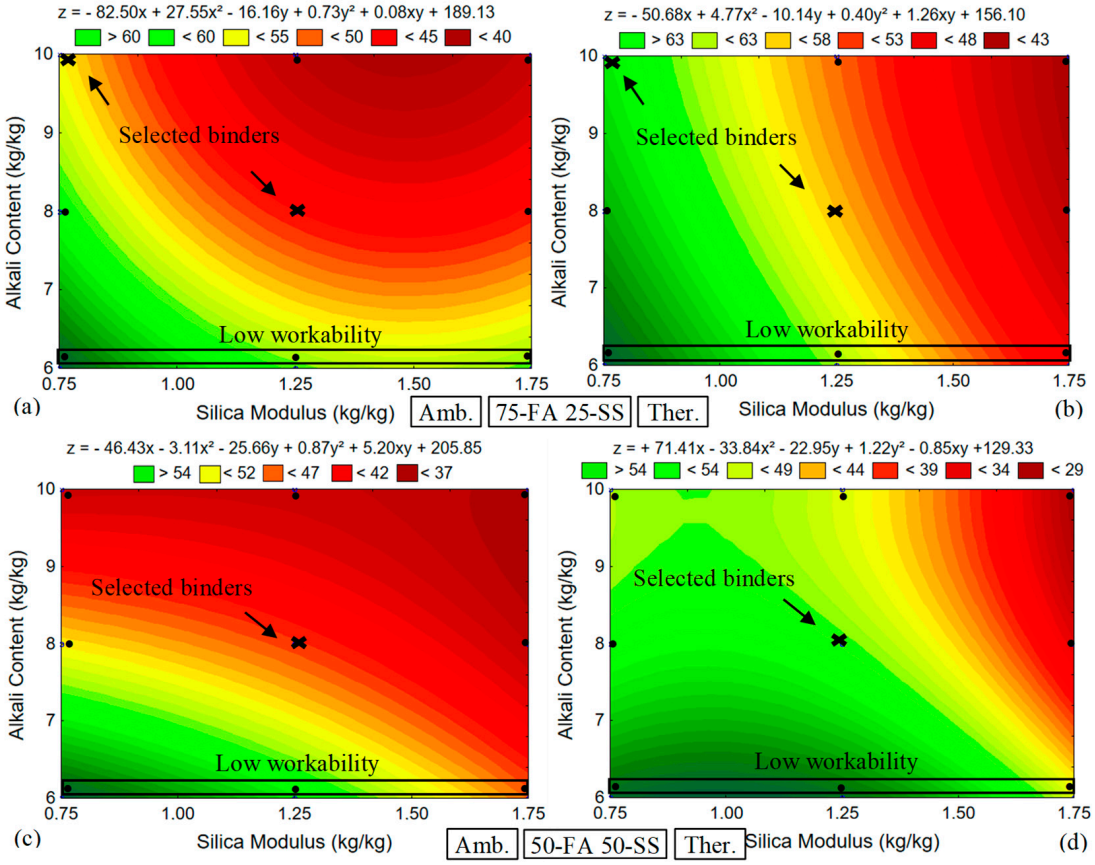

Figure 6. Compressive strength at 28 days of AAB pastes: (**a**) FA-SS 75%-25%, ambient cure (25 °C); (**b**) FA-SS 75%-25%, thermal cure (65 °C); (**c**) FA-SS 50%-50%, ambient cure (25 °C); (**d**) FA-SS 50%-50%, thermal cure (65 °C).

An increase in alkali content typically enhances compressive strength up to an optimal threshold, beyond which further increases may reduce performance due to excessive precursor dissolution and the formation of unstable reaction products [4,11]. In this study, the highest strength was observed at a 6% N/B ratio, indicating an optimal condition for geopolymerization, followed by lower performance at 8% and 10%. However, low liquid content at this ratio resulted in limited workability. To address this, the use of more diluted alkaline solutions, while maintaining the same total 6% N/B, could be explored to improve workability. Notably, the N/B and S/N exhibit a coupled effect, whereas their combined variation influences the mechanical behavior of the binder system.

Thermal curing further enhanced compressive strengths at S/N values of 0.75 and 1.25, with the highest performance at S/N of 0.75 and N/B of 10% attributed to increased alkalis and soluble silica availability. These results (Figure 6) highlight the importance of optimizing S/N and N/B ratios for BOF slag-based AABs, demonstrating their distinct reactivity compared to conventional precursors.

Statistical analysis using ANOVA confirmed the significance of S/N, N/B, precursor ratios, and curing conditions on compressive strength, with interactions between these variables also exhibiting statistical significance at a 95% confidence level (F = 1.585). Duncan's multiple range test identified binders 3, 5, and 11 as having no significant differences in performance, and these were selected for further analysis, including fresh-state properties and long-term strength evolution (Figure 6).

4.1.3. Paste Setting Time, Monotonic Flowability and Early Compressive Strength Results

The paste formulations selected based on the strength criterion were formulations 3, 5, and 11, as detailed in Table 3. These formulations were further evaluated through setting-time and mini-slump tests to assess fresh-state properties. The results for initial and final setting times are shown in Figure 7.

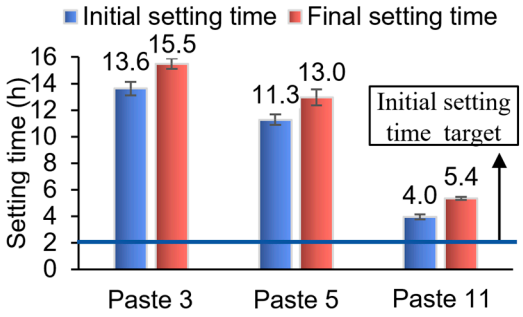

Figure 7. Setting time of AAB pastes 3, 5 and 11.

All paste formulations met the initial setting time requirement of a value higher than 45 min, in accordance with ASTM C191 [38]. Their final setting times were longer compared to Portland cement, which ranges between 2 and 3 h [38]. For in situ applications, this extended setting time offers greater flexibility during casting, particularly under environmental conditions such as elevated temperatures (>30 °C). The exothermic nature of the activator reactions, and variations in calcium content (CaO%) or mixing energy have a demonstrated influence on those outcomes [8,35,55]. The higher CaO% has an additional role in shortening the setting-time process [35,55,56].

Pastes 3 and 5 exhibited longer initial setting times, recorded at 13.6 and 11.3 h, respectively, compared to 4 h for Paste 11 (Figure 7). This significant reduction in Paste 11's setting time was attributed to its precursor ratio (FA-SS 50:50), as higher calcium content in the slag accelerates the initial setting process [35,55]. In contrast, the FA-dominant compositions of Pastes 3 and 5 (FA-SS 75:25) aligned with typical setting time behavior reported for FA-based AABs, where lower calcium content leads to delayed setting [35,55].

The AAB pastes' mini-slump test results, shown in Figure 8, demonstrated paste spreading diameters measured at 30, 90, and 300 s. The activator solution-to-binder precursor (A/B) ratios were 0.5, 0.45, and 0.40 for Pastes 3, 5, and 11, respectively. This test is distinct from the Abrams cone test performed for concretes. This demonstrates the influence of the mix design parameters on rheological properties and hardened states.

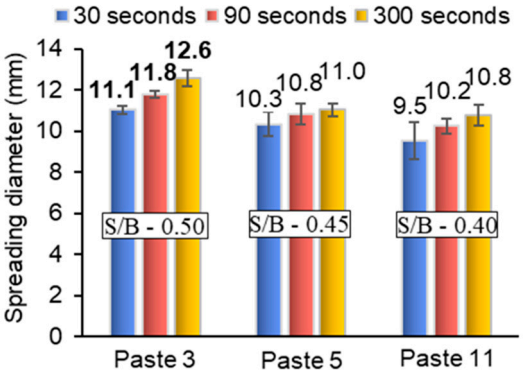

Figure 8. Spreading diameter by the mini-slump method, for AAB Pastes 3, 5 and 11.

Paste 3 exhibited the highest fluidity, with an initial spread diameter of 11.1 cm at 30 s and a final 12.6 cm at 300 s, with a good balance between high spread and satisfactory

mechanical properties, i.e., required compressive strength. In comparison, Hadi et al. [55] reported average spread values of 16.6 cm after 15 min for FA and blast furnace slag pastes with an activator-to-precursor ratio of 0.5.

The yield stress values were 5.6 Pa, 11.1 Pa, and 13.1 Pa for Pastes 3, 5, and 11, respectively, aligning with expectations as Paste 3 demonstrated the lowest yield stress due to its higher fluidity. The values in the literature for AAB pastes range between 0 and 200 Pa [42,57]. This enhanced fluidity is advantageous for self-compacting AAB concretes, facilitating void filling and contributing to a more cohesive structure. The compressive strength results for the AAB Pastes are presented in Figure 9.

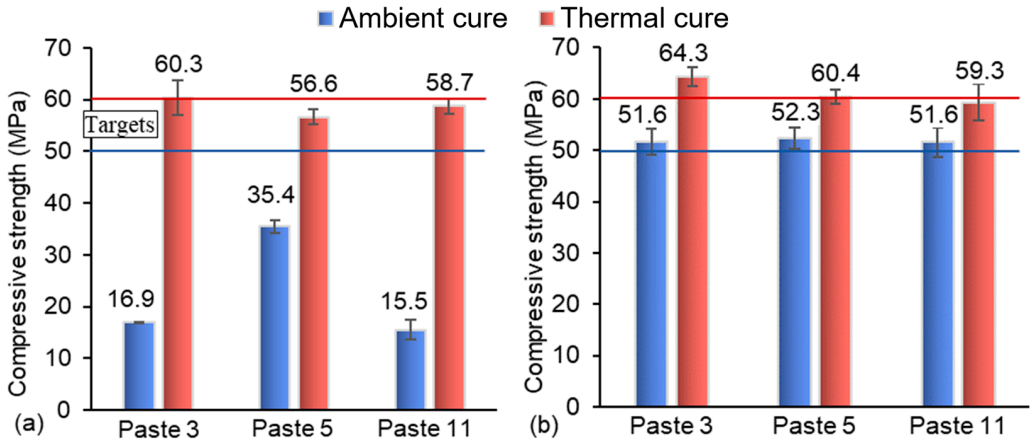

Figure 9. Compressive strength of AAB Pastes 3, 5 and 11 for (**a**) 7 days, (**b**) 28 days.

Paste 5 exhibited the highest early-age compressive strength under ambient curing conditions, which is attributed to the higher silica modulus (S/N = 1.25) of its activating solution, due to a greater proportion of sodium silicate in its composition. This high ratio increases the concentration of soluble silica, thereby enhancing early strength [52].

The thermal curing results showed no statistically significant increase in compressive strength between 7 and 28 days, aligning with observations in ambient curing. At 7 days, the compressive strength represented around 33% of the 28-day result across most formulations, except for Paste 5, achieving 66%. This is consistent with the literature indicating that early strength gain in alkali-activated systems is influenced by silica availability and reaction kinetics under varying curing conditions [8,35,55].

Slower strength development is observed in low-calcium systems, such as those based on FA, e.g., the formulation evaluated in this study. Paste 3 exhibited the highest fluidity, with its superior mini-slump spread and extended setting times, offering a broader casting time window [42,57]. Although Paste 5 reached higher early strength (7 days), Paste 3 was selected due to its lower sodium silicate demand, which contributes to reduced environmental impact and lower production cost. These characteristics are particularly beneficial for concrete applications, promoting efficient void filling and enhanced workability. Additional discussion on the influence of thermal curing is provided in Section 4.1.4.

4.1.4. AAB Paste Curing Conditions' Influence on Compressive Strength Evolution

Figure 10 illustrates the compressive strength time evolution for concrete produced with AAB Paste 3, highlighting the distinct strength evolution patterns under thermal and ambient curing conditions. Strength development was assessed at multiple time intervals (3, 7, 14, 28, 56, and 112 days) to evaluate the influence of curing methods and age on performance. Replicate specimens of Paste 3 were tested to ensure the consistency and reliability of the results.

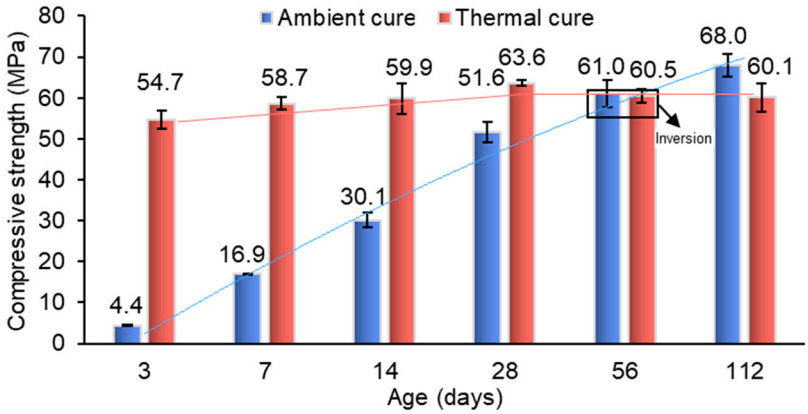

Figure 10. Compressive strength evolution of concrete made using AAB formulation 3.

Thermal curing is known for promoting high initial strength in AABs [9], as evidenced by compressive strength values exceeding the 50 MPa requirement by the third aging day, reaching 86% of the 28-day strength (63.6 MPa). However, a reduction in strength was observed over time, with a value of 60.1 MPa at 112 days. Thermal curing affects phase transitions during alkali activation by accelerating reaction kinetics and promoting gel formation of alkali-activated systems. However, this mechanism may also favor the generation of metastable phases that progressively decompose, potentially compromising long-term strength [17].

Another hypothesis for the observed strength reduction involves the transformation of amorphous gels into more ordered or crystalline zeolitic structures, which may trigger microstructural rearrangements and internal stress accumulation [29,58].

No statistically significant variation in strength was detected over time under thermal curing, a behavior likely influenced by material heterogeneity, microstructural inconsistencies, and casting-related variability. Nonetheless, the thermal curing regime demonstrated lower dispersion, as evidenced by a narrower confidence interval and improved homogeneity across specimens. Compressive strength beyond 112 days was not assessed due to practical constraints. Still, extended aging analyses remain necessary to properly evaluate long-term durability.

Ambient curing, conversely, favored positive strength evolution at later ages [59], possibly surpassing thermal curing results [11]. By 56 days, the ambient-cured specimens surpassed their thermal-cured counterparts, achieving 61 MPa, and reached 68 MPa at 112 days, contrary to the literature findings [8,14,34]. This behavior may be attributed to delayed geopolymerization. Under room temperature curing, the pores remain saturated for longer periods, allowing the gradual dissolution of unreacted particles. These particles continue to participate in the reaction, leading to microstructural refinement and strength development. As observed by [60,61], the early-age microstructure typically consists of porous aluminosilicate gels with unreacted particles dispersed throughout. Over time, these gels densify and additional reaction products fill the pores, reducing porosity and increasing compressive strength [62]. Further investigation is recommended to confirm this trend and better understand the mechanisms underlying long-term strength development in ambient-cured AABs.

4.1.5. AAB Paste Microstructural Analysis Based on SEM/EDS and XRD

Figure 11 shows SEM images of AAB Pastes 3, 5, and 11 under ambient curing. The three pastes exhibit distinct surface characteristics. Paste 11 presented a more homogeneous and denser microstructure, indicative of calcium-based gels such as C-A-S-H [5,6,9], likely due to its higher BOF slag content and lower activator-to-precursor ratio (0.4). In contrast,

Paste 3 showed a more porous structure, attributed to its higher activator-to-precursor ratio (ratio of 0.5) [14], which may reduce strength but improve workability. Pastes 3 and 5 also showed more areas with a granular or "sugary" appearance, possibly related to N-A-S-H gel formation [11].

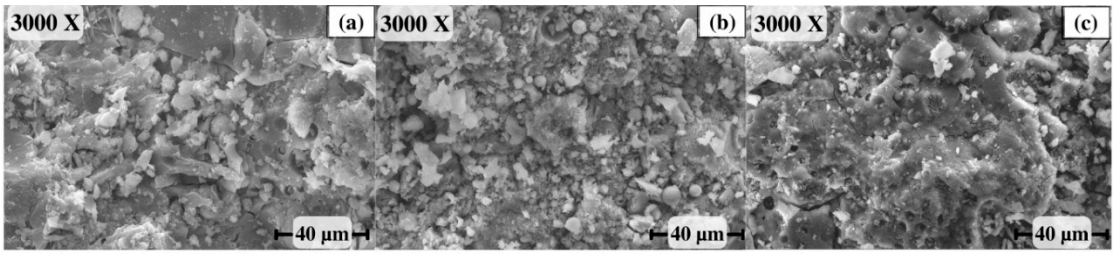

Figure 11. SEM images of AAB Pastes under ambient cure: (**a**) paste 3; (**b**) paste 5; (**c**) paste 11.

The alkali-to-binder ratio (N/B) is a critical parameter governing the dissolution of aluminosilicate precursors and the subsequent formation of reaction products. Insufficient alkali availability limits precursor activation, reducing gel yield and mechanical performance [63], whereas excessive alkali concentrations can result in the formation of secondary phases (e.g., efflorescence) and compromise the long-term microstructural integrity of the binder [64]. In the present study, an N/B of 6% produced the highest compressive strength values among the tested formulations, despite exhibiting poor workability. This value is consistent with those reported for BOF slag-based binders with N/B ratios around 4–6% [65].

The silica modulus (SiO_2/Na_2O) also exerts significant influence on the structure and chemistry of alkali-activated binders. Elevated silica modulus values enhance the availability of soluble silicates, promoting the formation of more polymerized and compact reaction gels [11]. In slag-rich systems—particularly those incorporating Basic Oxygen Furnace (BOF) slag with inherently low reactivity—moderate SiO_2/Na_2O ratios (1.50–2.22) are reported to optimize the formation of calcium-rich gels such as C–(A)–S–H [65]. Under ambient curing, higher silica moduli (e.g., 1.75) favored gel development and strength gain, while lower values (0.75–1.25) were more effective under thermal curing conditions, likely due to accelerated reaction kinetics. These effects are further examined in Section 4.2.

Figure 12 displays the microstructural features of the AAB Paste 3 cured under ambient conditions, as identified by SEM/EDS analysis, highlighting partially reacted FA and SS particles embedded within aluminosilicate gels. This microstructure is typical of FA-based AABs, where reaction products precipitate on precursor particle surfaces, altering their morphology. Over time, a network of interconnected gels forms, densifying the matrix and encapsulating both unreacted and partially reacted particles [66,67]. Voids observed in the paste are attributed to water release during gel condensation, which may be only partially eliminated during curing [68].

Spherical voids in the matrix are linked to FA hollow spheres, known as cenospheres, where reactions occur along the glassy shell surfaces. These reactions promote gel interconnection and the filling of interparticle voids, though some intraparticle voids remain unfilled. Consequently, the microstructure includes FA particles at varying reaction stages [13]. Notably, Figure 12 reveals unreacted FA spheres within spherical voids, indicating the presence of plerospheres—larger hollow spheres containing smaller ones—further emphasizing the dynamics of heterogeneous reactions [13]. This observation supports the hypothesis that fly ash-based matrices develop mechanical strength more progressively in the absence of thermal curing, i.e., ambient curing, as the reaction kinetics progress more slowly in the absence of thermal activation, delaying the formation and densification of the aluminosilicate gel matrix.

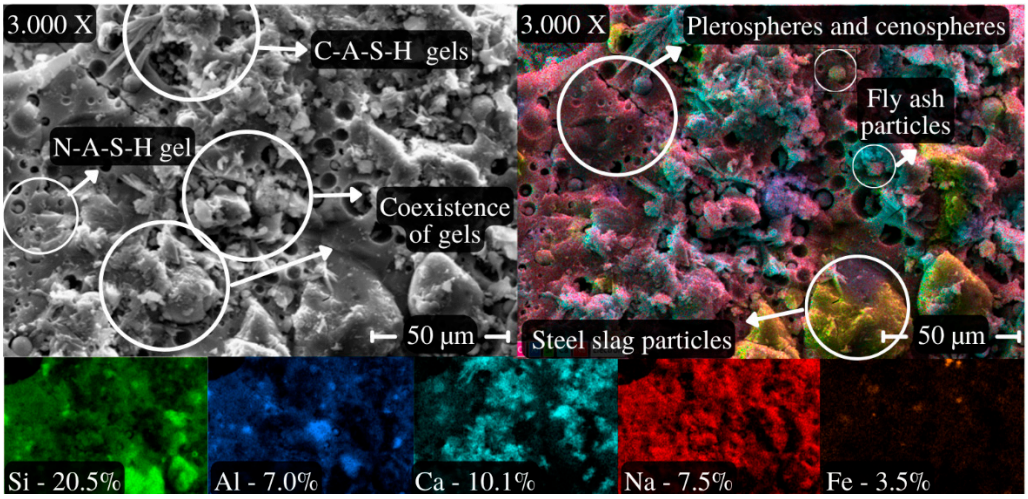

Figure 12. SEM/EDS characterization of gel phases in AAB Paste 3 under ambient curing.

The presence of plerospheres supports the long-term strength gain, as many smaller particles begin to dissolve only after the surrounding larger particle layer is degraded. This structure acts as a reservoir, gradually releasing chemical species that sustain geopolymerization over time [69].

The SEM/EDS analysis in Figure 12 identifies areas with higher calcium content (cyan), which can indicate the gel phases of C-A-S-H gels structures [70,71]. Regions with higher sodium content (red) and lower calcium content can suggest the formation of N-A-S-H gels, as suggested by Cristelo et al. [28] and ohers authors [9,35]. Areas exhibiting both high calcium and sodium content (light blue and red) imply the coexistence of C-A-S-H and N-A-S-H gels, highlighting a complex and interdependent gel matrix. Given the compositional overlap between gel phases, further characterization is required to improve the resolution and differentiation of the gel phases, elucidating structural and chemical distinctions.

Elemental analysis using EDS revealed atomic ratios of Ca/(Al+Si) and Ca/Si as 0.37 and 0.50, respectively. These values align with findings by Kamath, Prashanth, and Kumar [72], who reported Ca/Si ratios between 0.29 and 0.53 and Ca/(Al+Si) ratios between 0.19 and 0.39 in systems where N-A-S-H and C-A-S-H gels coexist. This balanced coexistence contributes to a dense and homogeneous microstructure, offering superior chemical resistance [12,13], enhanced compressive strength at elevated temperatures [14], and reduced porosity [6,13].

Figure 13 shows diffraction patterns of AAB obtained in another work [73] with the same composition as Paste 3, under ambient curing. The material exhibited peaks corresponding to silicon dioxide (SiO_2), calcium oxide (CaO), calcium iron silicate, and calcium iron oxide phases. The high concentrations of Ca and Fe promoted the formation of crystalline structures enriched with these metals, which influenced the observed structural characteristics and may be associated with C-A-S-H gels [28,74]. Unlike crystalline materials, N-A-S-H is predominantly amorphous, making its identification in XRD challenging. Instead of sharp peaks, N-A-S-H typically appears as one or more broad humps in the XRD pattern [75]. These broad humps, typically observed between 2θ values of 25° and 35°, are indicative of an amorphous or poorly crystalline material. The pattern shown in Figure 13 features an amorphous hump between 2θ values of 20° and 35°, suggesting the presence of this gel phase. This hypothesis is further supported by the SEM/EDS images, which show high sodium content in certain regions of the material.

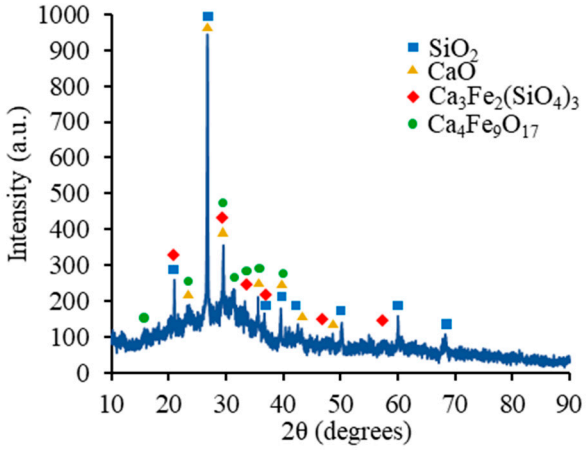

Figure 13. Diffraction patterns of a material similar to AAB Paste 3 under ambient curing [76].

Complementary insights from Mercury Intrusion Porosimetry (MIP) analyses indicated an average porosity of 9.4%, with the majority of voids (81.3%) falling within the 0.01 μm to 10 μm range, encompassing meso- and macropores. This aligns with those values reported for FA-GGBFS-based AABs, although it is slightly higher than those found in metakaolin-based systems, where finer pore structures are more prevalent, with pore sizes ranging between 1 and 5 nm [76].

4.2. Alkali-Activated Concrete Results

4.2.1. Fresh-State Self-Compacting AAB Concrete Characterization

The concrete mix with a paste content of 38.2% (i.e., void content plus 20% adjustment for optimal fluidity), achieved a slump value of 270 mm spread. It fulfills the self-compacting behavior requirement for the fresh state. The slump flow test yielded results of 575 ± 17 mm, while the T50 time was 13.8 ± 1.3 s, classifying the material as VS2 for viscosity and SF1 for flowability [43]. The Visual Stability Index (VSI) was zero, according to ASTM C1611 [46], with the absence of segregation or bleeding during testing. This stability was attributed to the high viscosity of the paste, which ensured uniform distribution and cohesion throughout the mixture [46].

4.2.2. AAB Concretes' Compressive Strength and Young's Modulus Results

The AAB concretes' exhibited an apparent density of 2305.6 kg/m^3. Compressive strength results for 7, 14, and 28 days under both curing methods are shown in Figure 14.

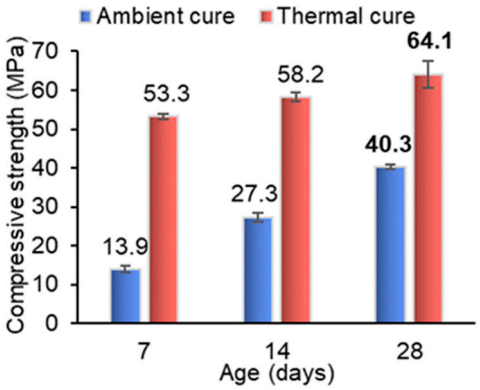

Figure 14. Compressive strength of AAB concretes at 28 days.

Thermal curing demonstrated higher early-age strength, with values increasing marginally over time, ranging from 53.3 MPa at 7 days to 64.1 MPa at 28 days. At 28 days,

compressive strength values for thermally cured specimens were comparable to those of the paste under similar curing conditions. Ambient curing, however, resulted in a 10 MPa reduction in compressive strength compared to the paste, which is due to the influence of the interfacial transition zone (ITZ), investigated in another study [73]. Thermal curing positively affected the ITZ, enhancing matrix–aggregate bonding, as reported in similar studies [7,39]. The compressive strength values for AAB concretes' exceeded those reported in the literature for self-compacting AAB concretes with steel slag, which are typically capped at 48 MPa [77–79].

The Young's modulus results were 20.2 GPa under ambient curing and 26.2 GPa under thermal curing. These values are lower than those typically reported for conventional Portland cement concretes (PCCs), which usually range from 30 to 35 GPa [80,81], and significantly below those of high-performance PCCs, which often reach between 50 and 60 GPa [82]. Nonetheless, this is consistent with previous findings indicating that AAB for concrete applications often exhibit a lower Young's modulus despite achieving high compressive strength values [83]. The type and proportion of gels formed during alkali activation, N-A-S-H and C-A-S-H gels, significantly influence Young's modulus. Low-calcium AAB formulations often yield lower values, ranging between 15 and 18 GPa [84]. Conversely, high-calcium AABs, such as those using slag-based precursors, achieve higher Young's modulus values (12–47 GPa). This behavior is attributed to the predominance of C-A-S-H gels, which are similar to those formed during the hydration of Portland cement [18,84].

Waqas et al. [85] reported Young's modulus values between 14.5 GPa and 31.2 GPa for FA-GGBS based AABs, with modulus increasing proportionally with slag content due to higher calcium oxide availability. Ding et al. [18] observed values of 22.7 GPa and 27.4 GPa for AABs composed of 50:50 FA-slag ratio, which were lower than Portland cement concrete with similar compressive strengths. The results of this study align with these findings, underscoring the variability in Young's modulus due to differences in material composition and gel structure arising from the calcium content of precursors.

Adjustments to calcium content or the use of aggregates with higher stiffness could further increase the Young's modulus [18,78,86]. The high compressive strength and self-compacting behavior of the AAB concretes', combined with its superior passing ability, demonstrate its potential for technical applications

In conclusion, alkali-activated concrete (AAC) stands out as a feasible and technically robust alternative to Portland cement concrete (PCC). When strategically formulated, AAC can deliver high compressive strength, as demonstrated in this study by values exceeding those typically reported for steel slag-based systems, while maintaining self-compacting properties and superior passing ability. Also, the microstructure analysis indicated potential long-term durability [3,8,13,17].

One major gap to alkali-activated concrete large-scale adoption lies in having a rheological behavior close to conventional concretes. Those outcomes addressed this challenge through a systematic mix design methodology incorporating particle packing and parametric optimization, enabling fluidity and workability to meet standard construction constraints [8]. Although the measured Young's modulus remained lower, this outcome aligns with the established behavior of AAB systems, where hybrid gel formations (N-A-S-H and C-A-S-H) offer strength and cohesion even without equivalent stiffness.

Furthermore, ambient-cured specimens displayed strength development over time, supporting the feasibility of non-thermal curing pathways, with stronger environmental appeal. With a reduced reliance on sodium silicate, the material affirms its status as a sustainable and technically viable solution for future structural applications.

Alkali-activated binders can exhibit the coexistence of C-A-S-H and N-A-S-H gels, which are characteristic of high- and low-calcium systems, respectively [5,6,9]. This combination contributes to the superior chemical resistance of N-A-S-H and the low porosity of C-A-S-H [5,6,9]. Therefore, when properly proportioned, AAB concretes can offer superior strength and durability compared to PCC [85]. Moreover, the use of AAB presents an excellent opportunity for valorizing industrial waste, thereby promoting a circular economy. The AAB had a potential for 55% to 75% CO_2 emissions reduction compared to PCC [87]. Both alkali-activated concrete binders and Portland cement binders have their advantages and disadvantages, making it essential to consider the specific requirements of their application, including mechanical properties, workability, and exposure conditions.

5. Conclusions

This study investigated the microstructural, mechanical and fresh-state performance of alkali-activated binders incorporating BOF steel slag, aiming to optimize their use and validate their potential as viable precursors in concrete applications. A proof of concept was established by demonstrating the feasibility of producing alkali-activated concretes with adequate rheological control, compressive strength, and setting time.

The parametric methodology systematically investigated the effects of silica modulus (S/N), alkali content (N/B), precursor ratios, and curing conditions on key performance parameters. Through response surface modeling and aggregate packing design, the proposed mix design method enabled the formulation of high-performance binders with reduced viscosity, enhanced workability, and compressive strength suitable for self-compacting and high-performance structural composites. These findings reinforce the practical and structural potential of BOF slag-based AABs when supported by systematic design strategies. The yielded insights and implications encompass the following:

- A lower S/N parameter (0.75) demonstrated higher compressive strength results. This result differs from the findings often presented in the literature, where FA and GGBFS-based AAB usually exhibit optimal S/N ratios between 1.25 and 1.75;
- Thermal curing increased compressive strength at early ages, with results exceeding 50 MPa by 3 days and reaching 63.6 MPa at 28 days, but formulations with higher S/N (1.75) showed limited benefits, suggesting the need for parameter-specific adjustments;
- Ambient-cured AAB pastes demonstrated progressive strength development, surpassing thermally cured specimens at later ages (e.g., 68 MPa at 112 days), highlighting the viability of this lower-energy and more sustainable curing strategy;
- AAB concretes exhibited lower Young's modulus values compared to what is expected for Portland cement concretes with similar strength levels and aggregates, consistent with the geopolymer literature. The modulus ranged from 20.2 GPa (ambient curing) to 26.2 GPa (thermal curing), influenced by the coexistence of N-A-S-H and C-A-S-H gels and the precursor's calcium content;
- The microstructures of the AABs were dense and homogeneous as compared to conventional concretes, and were characterized by low porosity (9.4%) and optimal gel proportions.

These findings contribute to the advancement of research on industrial waste valorization, particularly fly ash and steel slag, offering viable alternatives to Portland cement in regions where suitable precursors for AAB are available. The designed materials demonstrate significant potential for precast applications, where controlled casting and curing conditions favor their performance.

Author Contributions: Conceptualization, L.B.R.A., D.L.L.T. and L.F.A.L.B.; methodology, L.B.R.A., D.L.L.T. and H.N.C.; validation, L.F.A.L.B.; formal analysis, H.N.C.; investigation L.B.R.A., D.L.L.T. and L.F.A.L.B.; resources, L.F.A.L.B., D.L.L.T., A.E.B.C. and H.N.C.; data curation, L.B.R.A., D.L.L.T. and L.F.A.L.B.; writing—original draft preparation, L.B.R.A. and D.L.L.T.; writing—review and editing, all authors; visualization, all authors.; supervision, L.F.A.L.B., A.E.B.C. and J.B.S.B.; project administration, L.F.A.L.B., A.E.B.C., J.B.S.B. and H.N.C.; funding acquisition, L.F.A.L.B. and A.E.B.C. All authors have read and agreed to the published version of the manuscript.

Funding: This research has received funding from the European Union's Horizon 2020 research and innovation program under the Marie Skłodowska-Curie COFUND grant agreement No. 101034248. This research was supported by the following institutions: Coordination for the Improvement of Higher Education Personnel (CAPES) and the National Council for Scientific and Technological Development (CNPq), project numbers: 312817/2020-7; 409236/2022-5; 308888/2020-0.

Data Availability Statement: The data referenced in this study are accessible upon formal request to the corresponding author.

Acknowledgments: The research presented in this article has contributed to the development of two patents: "Mix Design Method for Geopolymeric Binders: application on products based on Coal Ashes and Steel Slags" (Patent No. INPI BR 102022019303-7, filed/granted on 5 March 2024) and "High-Workability Concrete with Alkali-Activated Binders and Steel Slag Aggregates, and its Production Method" (Patent No. INPI BR 102022023033-1, filed/granted on 11 March 2025). The authors acknowledge this outcome as a continuation of the scientific advancements discussed in this study.

Conflicts of Interest: The authors declare no conflict of interest.

References

1. Delgado, J.M.D.; Oyedele, L.; Ajayi, A.; Akanbi, L.; Akinade, O.; Bilal, M.; Owolabi, H. Robotics and automated systems in construction: Understanding industry-specific challenges for adoption. *J. Build. Eng.* **2019**, *26*, 100868. [CrossRef]
2. Baic, I.R.; Kozioł, W.; Miros, A. Dependence of extraction and production of construction aggregates on selected indicators of economic development in Poland. *Arch. Civ. Eng.* **2021**, *67*, 437–453. [CrossRef]
3. Singh, N.B.; Middendorf, B. Geopolymers as an alternative to Portland cement: An overview. *Constr. Build. Mater.* **2019**, *237*, 117455. [CrossRef]
4. Li, N.; Shi, C.; Zhang, Z.; Zhu, D.; Hwang, H.J.; Zhu, Y.; Sun, T. A mixture proportioning method for the development of performance-based alkali-activated slag-based concrete. *Cem. Concr. Comp.* **2018**, *93*, 163–174. [CrossRef]
5. Provis, J.L. Geopolymers and other alkali activated materials: Why, how, and what? *Mater. Struct.* **2014**, *47*, 11–25. [CrossRef]
6. Provis, J.L.; Bernal, S.A. Geopolymers and related alkali-activated materials. *Annu. Rev. Mater. Res.* **2014**, *44*, 299–327. [CrossRef]
7. Farooq, F.; Jin, X.; Javed, M.F.; Akbar, A.; Shah, M.I.; Aslam, F.; Alyousef, R. Geopolymer concrete as sustainable material: A state of the art review. *Constr. Build. Mater.* **2021**, *306*, 124762. [CrossRef]
8. Xie, T.; Visintin, P.; Zhao, X.; Gravina, R. Mix design and mechanical properties of geopolymer and alkali activated concrete: Review of the state-of-the-art and the development of a new unified approach. *Constr. Build. Mater.* **2020**, *256*, 119380. [CrossRef]
9. Provis, J.L.; Van Deventer, J.S.J. (Eds.) *Alkali Activated Materials: State-of-the-Art Report, RILEM TC 224-AAM*; RILEM State-of-the-Art Reports; Springer: Dordrecht, The Netherlands, 2014; Volume 13, ISBN 978-94-007-7671-5.
10. Li, N.; Shi, C.; Zhang, Z.; Wang, H.; Liu, Y. A review on mixture design methods for geopolymer concrete. *Comp. Part B Eng.* **2019**, *178*, 107490. [CrossRef]
11. Soutsos, M.; Boyle, A.P.; Vinai, R.; Hadjierakleous, A.; Barnett, S.J. Factors influencing the compressive strength of fly ash based geopolymers. *Constr. Build. Mater.* **2016**, *110*, 355–368. [CrossRef]
12. Zhang, J.; Shi, C.; Zhang, Z.; Ou, Z. Durability of alkali-activated materials in aggressive environments: A review on recent studies. *Constr. Build. Mater.* **2017**, *152*, 598–613. [CrossRef]
13. Bernal, S.A.; Provis, J.L. Durability of alkali-activated materials: Progress and perspectives. *J. Am. Ceram. Soc.* **2014**, *97*, 997–1008. [CrossRef]
14. Zhang, P.; Wang, K.; Li, Q.; Wang, J.; Ling, Y. Fabrication and engineering properties of concretes based on geopolymers/alkali-activated binders-A review. *J. Clean. Prod.* **2020**, *258*, 120896. [CrossRef]
15. Lee, N.K.; Lee, H.K. Setting and mechanical properties of alkali-activated fly ash/slag concrete manufactured at room temperature. *Constr. Build. Mater.* **2013**, *47*, 1201–1209. [CrossRef]

16. Rafeet, A.; Vinai, R.; Soutsos, M.; Sha, W. Guidelines for mix proportioning of fly ash/GGBS based alkali activated concretes. *Constr. Build. Mater.* **2017**, *147*, 130–142. [CrossRef]
17. Thomas, R.J.; Peethamparan, S. Stepwise regression modeling for compressive strength of alkali-activated concrete. *Constr. Build. Mater.* **2017**, *141*, 315–324. [CrossRef]
18. Ding, Y.; Shi, C.-J.; Li, N. Fracture properties of slag/fly ash-based geopolymer concrete cured in ambient temperature. *Constr. Build. Mater.* **2018**, *190*, 787–795. [CrossRef]
19. Bondar, D.; Nanukuttan, S.; Provis, J.L.; Soutsos, M. Efficient mix design of alkali-activated slag concretes based on packing fraction of ingredients and paste thickness. *J. Clean. Prod.* **2019**, *218*, 438–449. [CrossRef]
20. Zhong, Q.; Su, M.; Tian, X.; Peng, H. Workability and mechanical properties for GGBFS–MK geopolymer synthesis: Influencing factor analysis and a mix design method. *Mater. Struct.* **2023**, *56*, 144. [CrossRef]
21. Naidu, T.S.; Sheridan, C.M.; Van Dyk, L.D. Basic oxygen furnace slag: Review of current and potential uses. *Miner. Eng.* **2020**, *149*, 106234. [CrossRef]
22. Nunes, V.A.; Borges, P.H.R. Recent advances in the reuse of steel slags and future perspectives as binder and aggregate for alkali-activated materials. *Constr. Build. Mater.* **2021**, *281*, 122605. [CrossRef]
23. Crude Steel Production and 2021 Global Crude Steel Production Totals. December 2021. Available online: https://worldsteel.org/ (accessed on 9 June 2025).
24. Horii, K.; Kato, T.; Sugahara, K.; Tsutsumi, N.; Kitano, Y. Overview of iron/steel slag application and development of new utilization technologies. *Nippon. Steel Sumitomo Tech. Rep.* **2015**, *109*, 5–11.
25. Elahi, M.M.A.; Hossain, M.M.; Karim, M.R.; Zain, M.F.M.; Shearer, C. A review on alkali-activated binders: Materials composition and fresh properties of concrete. *Constr. Build. Mater.* **2020**, *260*, 119788. [CrossRef]
26. Jin, S.; Zhao, Z.; Jiang, S.; Sun, J.; Pan, H.; Jiang, L. Comparison and summary of relevant standards for comprehensive utilization of fly ash at home and abroad. *IOP Conf. Ser. Earth Environ. Sci.* **2021**, *621*, 012006. [CrossRef]
27. Song, W.; Zhu, Z.; Peng, Y.; Wan, Y.; Xu, X.; Pu, S.; Song, S.; Wei, Y. Effect of steel slag on fresh, hardened and microstructural properties of high-calcium fly ash based geopolymers at standard curing condition. *Constr. Build. Mater.* **2019**, *229*, 116933. [CrossRef]
28. Cristelo, N.; Coelho, J.; Miranda, T.; Palomo, Á.; Fernández-Jiménez, A. Alkali activated composites–An innovative concept using iron and steel slag as both precursor and aggregate. *Cem. Concr. Comp.* **2019**, *103*, 11–21. [CrossRef]
29. Adesanya, E.; Ohenoja, K.; Kinnunen, P.; Illikainen, M. Properties and durability of alkali-activated ladle slag. *Mater. Struct.* **2017**, *50*, 255. [CrossRef]
30. Nassar, A.K.; Kathirvel, P. Effective utilization of agricultural waste in synthesizing activator for sustainable geopolymer technology. *Constr. Build. Mater.* **2022**, *362*, 129681. [CrossRef]
31. Nassar, A.K.; Kathirvel, P.; Murali, G.; Alqemlas, T.; Azab, M. Innovative one-part Alkali activated binder from activator derived from agricultural waste: Synthesis and application for sustainable construction. *Results Eng.* **2024**, *22*, 101975. [CrossRef]
32. *ASTM C618*; Standard Specification for Coal Fly Ash and Raw or Calcined Natural Pozzolan for Use as a Mineral Admixture in Concrete. American Society For Testing And Materials: West Conshohocken, PA, USA, 2019.
33. Yusuf, M.O.; Johari, M.A.M.; Ahmad, Z.A.; Maslehuddin, M. Evolution of alkaline activated ground blast furnace slag–ultrafine palm oil fuel ash based concrete. *Mater. Des.* **2014**, *55*, 387–393. [CrossRef]
34. Gomes, P.C.C.; Barros, A.R. *Métodos de Dosagem de Concreto Autoadensável*; PINI: São Paulo, Brazil, 2009.
35. Nath, P.; Sarker, P.K. Effect of GGBFS on setting, workability and early strength properties of fly ash geopolymer concrete cured in ambient condition. *Constr. Build. Mater.* **2014**, *66*, 163–171. [CrossRef]
36. Costa, H.N. Cimentos Álcali-Ativados à Base de Cinzas do Carvão Mineral e de Escórias Siderúrgicas. Ph.D. Thesis, Engineering and Materials Science Program, Federal University of Ceará, Fortaleza, Brazil, 2022.
37. *ABNT NBR 7.212*; Ready-Mixed Concrete—Preparation, Supply and Control. Associação Brasileira De Normas Técnicas: Rio de Janeiro, Brazil, 2021.
38. *ASTM C191*; Standard Test Methods for Time of Setting of Hydraulic Cement by Vicat Needle. American Society for Testing and Materials: West Conshohocken, PA, USA, 2021.
39. Luo, Z.; Li, W.; Wang, K.; Castel, A.; Shah, S.P. Comparison on the properties of ITZs in fly ash-based geopolymer and Portland cement concretes with equivalent flowability. *Cem. Concr. Res.* **2021**, *143*, 106392. [CrossRef]
40. Tavares, M.L.; Targino, D.L.L.; Cabral, A.E.B.; Nogueira, H. Evaluation of the effect of curing conditions on compressive strength and microstructure of alkali-activated binders. *Labor Eng.* **2024**, *18*, e024006. [CrossRef]
41. Roussel, N.; Coussot, P. "Fifty-cent rheometer" for yield stress measurements: From slump to spreading flow. *J. Rheol.* **2005**, *49*, 705–718. [CrossRef]
42. Tan, Z.; Bernal, S.A.; Provis, J.L. Reproducible mini-slump test procedure for measuring the yield stress of cementitious pastes. *Materials and Struct.* **2017**, *50*, 235. [CrossRef]

43. European Federation of National Associations Representing for Concrete (EFNARC). *European Guidelines for Self-Compacting Concrete: Specification, Production and Use, EFNARC—Publication Index | NBS*; EFNARC (European Federation of National Associations Representing for Concrete): Flums, Switzerland, 2005; p. 68.
44. Bernal, S.A.; De Gutiérrez, R.M.; Pedraza, A.L.; Provis, J.L.; Rodriguez, E.D.; Delvasto, S. Effect of binder content on the performance of alkali-activated slag concretes. *Cem. Concr. Res.* **2011**, *41*, 1–8. [CrossRef]
45. *ASTM C143*; Standard Test Method for Slump of Hydraulic-Cement Concrete. American Society For Testing And Materials: West Conshohocken, PA, USA, 2015.
46. *ASTM C1611*; Standard Test Method for Slump Flow of Self-Consolidating Concrete. American Society For Testing And Materials: West Conshohocken, PA, USA, 2010.
47. *ASTM C349*; Standard Test Method for Compressive Strength of Hydraulic-Cement Mortars (Using Portions of Prisms Broken in Flexure). American Society For Testing And Materials: West Conshohocken, PA, USA, 2018.
48. *ASTM C39*; Standard test method for compressive strength of cylindrical concrete specimens. American Society For Testing And Materials: West Conshohocken, PA, USA, 2020.
49. *ASTM C469*; Standard Test Method for Static Modulus of Elasticity and Poisson's Ratio of Concrete in Compression. American Society for Testing and Materials: West Conshohocken, PA, USA, 2022.
50. Bellum, R.R.; Reddy, K.H.K.; Reddy, G.C.; Reddy, M.R.K.; Gamini, S. Influence of steel slag on strength and microstructural characteristics of fly ash-based geopolymer concrete. *Multiscale and Multidisciplinary Modeling, Exp. Des.* **2024**, *7*, 5499–5514. [CrossRef]
51. Guo, X.; Pan, X. Mechanical properties and mechanisms of fiber reinforced fly ash–steel slag based geopolymer mortar. *Constr. Build. Mater.* **2018**, *179*, 633–641. [CrossRef]
52. Lee, W.H.; Cheng, T.W.; Lin, K.Y.; Lin, K.L.; Wu, C.C.; Tsai, C.T. Geopolymer technologies for stabilization of basic oxygen furnace slags and sustainable application as construction materials. *Sustainability* **2020**, *12*, 5002. [CrossRef]
53. Mcalexander, M.; Bharadwaj, K.; Weiss, J.W.; Isgor, O.B. Reactivity of waterglass in cementitious systems. *Cement* **2023**, *12*, 100067. [CrossRef]
54. Choi, S.C.; Lee, W.K. Effect of Fe_2O_3 on the physical property of geopolymer paste. In: Advanced materials research. *Adv. Mater. Res.* **2012**, *586*, 126–129. [CrossRef]
55. Hadi, M.N.S.; Zhang, H.; Parkinson, S. Optimum mix design of geopolymer pastes and concretes cured in ambient condition based on compressive strength, setting time and workability. *J. Build. Eng.* **2019**, *23*, 301–313. [CrossRef]
56. Geddes, D.A.; Walkley, B.; Matsuda, T.; Provis, J.P. Multi-year cementitious hydrate product formation in non-Portland high performance concretes. *Cement* **2024**, *18*, 100111. [CrossRef]
57. Dai, X.; Aydin, S.; Yardimci, M.Y.; Sun, Y.; Schutter, G. Effect of temperature on the fresh and hardened state properties of alkali-activated slag/fly ash mixtures. *Mater. Struct.* **2023**, *56*, 107. [CrossRef]
58. Ma, G.; Yan, Y.; Zhang, M.; Sanjayan, J. Effect of Steel Slag on 3d Concrete Printing of Geopolymer with Quaternary Binders. *Ceram. Int.* **2016**, *48*, 26233–26247. [CrossRef]
59. Lee, W.H.; Wang, J.H.; Ding, Y.C.; Cheng, T.W. A study on the characteristics and microstructures of GGBS/FA based geopolymer paste and concrete. *Constr. Build. Mater.* **2019**, *211*, 807–813. [CrossRef]
60. Huang, G.; Huang, Y.; Zheng, X.; Zhang, F.; Xu, J.; Qi, J.; Chen, Z. Study on the Characteristics of Crystal Formation and Transformation of Alkali-Activated Slag Minerals Induced by Weak Alkali. *Crystals* **2024**, *14*, 1231. [CrossRef]
61. Zhu, C.; Wan, Y.; Wang, L.; Ye, Y.; Yu, H.; Yang, J. Strength Characteristics and Microstructure Analysis of Alkali-Activated Slag–Fly Ash Cementitious Material. *Materials* **2022**, *15*, 5998. [CrossRef] [PubMed]
62. Bahmani, H.; Mostofinejad, D. High-performance concrete based on alkaline earth metal ions-activated slag at ambient temperature: Mechanical and microstructure properties. *J. Mater. Res. Technol.* **2023**, *24*, 4192–4207. [CrossRef]
63. Li, N.; Shi, C.; Wang, Q.; Zhang, Z. Composition design and performance of alkali-activated cements. *Mater. Struct.* **2017**, *50*, 178. [CrossRef]
64. Turkoglu, M.; Bayraktar, O.Y.; Benli, A.; Kaplan, G. Effect of cement clinker type, curing regime and activator dosage on the performance of one-part alkali-activated hybrid slag/clinker composites. *J. Build. Eng.* **2023**, *68*, 106164. [CrossRef]
65. Nunes, V.A.; Suraneni, P.; Bezerra, A.C.; Thomas, C.; Borges, P.H. Influence of activation parameters on the mechanical and microstructure properties of an alkali-activated BOF steel slag. *Appl. Sci.* **2022**, *12*, 12437. [CrossRef]
66. Fang, Y.; Kayali, O. The fate of water in fly ash-based geopolymers. *Constr. Build. Mater.* **2013**, *39*, 89–94. [CrossRef]
67. Puligilla, S.; Mondal, P. Role of slag in microstructural development and hardening of fly ash-slag geopolymer. *Cem. Concr. Res.* **2013**, *43*, 70–80. [CrossRef]
68. Lloyd, R.R.; Provis, J.L.; Smeaton, K.J.; Van Deventer, J.S. Spatial distribution of pores in fly ash-based inorganic polymer gels visualised by Wood's metal intrusion. *Microporous Mesoporous Mater.* **2009**, *126*, 32–39. [CrossRef]

69. Valentim, B.; Flores, D.; Guedes, A.; Shreya, N.; Paul, P.; Colin, R. Ward Notes on the occurrence of char plerospheres in fly ashes derived from Bokaro and Jharia coals (Jharkhand, India) and the influence of the combustion conditions on their genesis. *Int. J. Coal Geol.* **2016**, *158*, 29–43. [CrossRef]
70. García-Lodeiro, I.; Palomo, A.; Fernández-Jiménez, A.; Macphee, D.E. Compatibility studies between NASH and CASH gels. Study in the ternary diagram Na_2O–CaO–Al_2O_3–SiO_2–H_2O. *Cem. Concr. Res.* **2011**, *41*, 923–931. [CrossRef]
71. Zhu, X.; Li, W.; Du, Z.; Zhou, S.; Zhang, Y.; Li, F. Recycling and utilization assessment of steel slag in metakaolin based geopolymer from steel slag by-product to green geopolymer. *Constr. Build. Mater.* **2021**, *305*, 124654. [CrossRef]
72. Kamath, M.; Prashanth, S.; Kumar, M. Micro-characterisation of alkali activated paste with fly ash-GGBS-metakaolin binder system with ambient setting characteristics. *Constr. Build. Mater.* **2021**, *277*, 122323. [CrossRef]
73. Araújo, L.B.R.; Targino, D.L.; Babadopulos, L.F.A.L.; Fabbri, A.; Cabral, A.E.B.; Chehade, R.; Costa, H.N. Impact of Curing Temperature and Steel Slag Aggregates on High-Strength Self-Compacting Alkali-Activated Concrete. *Buildings* **2025**, *15*, 457. [CrossRef]
74. Lin, C.; Liu, Z.; Gao, Y.; Li, Z.; Zhang, J.; Niu, H. Study on the effect and mechanism of cement-based material retarder on red mud-based hybrid alkali activated cement. *J. Build. Eng.* **2023**, *70*, 106353. [CrossRef]
75. Wang, Q.; Li, H.; Ding, Z.; Shan, R.; Zhao, M. Construction of a Molecular Dynamics Model of NASH Geopolymer Based on XRD Analysis. *Materials* **2024**, *17*, 6103. [CrossRef]
76. Izadifar, M.; Valencia, N.C.; Xiao, P.; Ukrainczyk, N.; Koenders, E. 3D off-lattice coarse-grained Monte Carlo simulations for nucleation of alkaline aluminosilicate gels. *Materials* **2023**, *16*, 1863. [CrossRef] [PubMed]
77. Saini, G.; Vattipalli, U. Assessing properties of alkali activated GGBS based self-compacting geopolymer concrete using nano-silica. *Case Stud. Constr. Mater.* **2020**, *12*, e00352. [CrossRef]
78. Huseien, G.F.; Sam, A.R.M.; Alyousef, R. Texture, morphology and strength performance of self-compacting alkali-activated concrete: Role of fly ash as GBFS replacement. *Constr. Build. Mater.* **2021**, *270*, 121368. [CrossRef]
79. Zheng, Z.; Deng, P. Mechanical and fracture properties of slag/steel slag-based geopolymer fully recycled aggregate concrete. *Constr. Build. Mater.* **2024**, *413*, 134533. [CrossRef]
80. Katman, H.Y.B.; Khai, W.J.; Bheel, N.; Kırgız, M.S.; Kumar, A.; Khatib, J.; Benjeddou, O. Workability, Strength, Modulus of Elasticity, and Permeability Feature of Wheat Straw Ash-Incorporated Hydraulic Cement Concrete. *Buildings* **2022**, *12*, 1363. [CrossRef]
81. Bezerra, A.K.; Melo, A.R.; Freitas, I.L.; Babadopulos, L.F.; Carret, J.C.; Soares, J.B. Determination of modulus of elasticity and Poisson's ratio of cementitious materials using S-wave measurements to get consistent results between static, ultrasonic and resonant testing. *Constr. Build. Mater.* **2023**, *398*, 132456. [CrossRef]
82. Bahmani, H.; Mostofinejad, D. Microstructure of Ultra-High-Performance Concrete (UHPC)—A Review Study. *J. Build. Eng.* **2022**, *50*, 104118. [CrossRef]
83. Nath, P.; Sarker, P.K. Flexural strength and elastic modulus of ambient-cured blended low-calcium fly ash geopolymer concrete. *Constr. Build. Mater.* **2017**, *130*, 22–31. [CrossRef]
84. Němeček, J.; Šmilauer, V.; Kopecký, L. Nanoindentation characteristics of alkali-activated aluminosilicate materials. *Cem. Concr. Comp.* **2011**, *33*, 163–170. [CrossRef]
85. Waqas, R.M.; Butt, F.; Zhu, X.; Jiang, T.; Tufail, R.F.A. Comprehensive Study on the Factors Affecting the Workability and Mechanical Properties of Ambient Cured Fly Ash and Slag Based Geopolymer Concrete. *Appl. Sci.* **2021**, *11*, 8722. [CrossRef]
86. Palankar, N.; Ravi, S.A.U.; Mithun, B.M. Investigations on Alkali-Activated Slag/Fly Ash Concrete with steel slag coarse aggregate for pavement structures. *Int. J. Pavement Eng.* **2017**, *18*, 500–512. [CrossRef]
87. Yang, K.H.; Song, J.K.; Song, K.I. Assessment of CO_2 reduction of alkali-activated concrete. *J. Clean. Prod.* **2012**, *39*, 265–272. [CrossRef]

Disclaimer/Publisher's Note: The statements, opinions and data contained in all publications are solely those of the individual author(s) and contributor(s) and not of MDPI and/or the editor(s). MDPI and/or the editor(s) disclaim responsibility for any injury to people or property resulting from any ideas, methods, instructions or products referred to in the content.